Journal of Marine Science and Application (2026) 25: 1252-1271
https://doi.org/10.1007/s11804-025-00741-1

RESEARCH ARTICLE

Damage Effect of a Multi-cabin Structure Under Near-field Underwater Explosion

Shangjian Lin[1], Jinxiang Wang[1], Lingquan Kong[1], Jian Wang[1], Kui Tang[1], Yuanbo Li[1] and Yunkun Hou[1]

Received: 07 April 2025 / Accepted: 20 June 2025
© Harbin Engineering University and Springer-Verlag GmbH Germany, part of Springer Nature 2026

Abstract

Studying the damage effects of multi-cabin structures (MCS) subjected to underwater explosions holds immense significance for ship protection. Employing a combined experimental and numerical simulation approach, this paper comprehensively investigates the damage effects of MCS under near-field underwater explosion. Three distinct damage modes are defined. Damage results of MCS caused by a single explosive and simultaneous detonation of two explosives with equivalent total mass are analyzed. A damage factor designated F^* is proposed for determining the MCS damage mode under simultaneous dual-explosive detonation. The three different damage modes of MCS are as follows: I) Plastic deformation of the outermost layer; II) Tearing failure of the outermost layer accompanied by significant deformation of the second layer; III) Tearing failure of both the outermost and second layers. Once a breach occurs in the first layer, a water jet penetrates into the cabin and strikes the second layer, causing secondary damage. Additionally, the fragments generated from the first layer colliding with the second layer are the primary factors contributing to the occurrence of Mode III. The study presents criteria for distinguishing these three damage modes based on different shock wave impact locations. When damage factor $F^* \geqslant 1$, MCS experiences damage in Mode II; whereas when $F^* < 1$, MCS undergoes damage in Mode I. F^* achieves 96.5% accuracy in damage mode prediction for MCS under 250 g−1 080 g TNT charges. When the total mass of explosives remains constant, the simultaneous explosion of two explosives exerts a more pronounced damage effect on MCS than a single explosive.

Keywords Underwater explosion; Multi-cabin structure; Synchronous detonation; Plastic deformation; Damage mechanism; Damage factor

1 Introduction

With the thriving global ocean economy, activities such as maritime transportation and offshore resource development have become increasingly frequent. The safety and durability of various marine engineering structures, including oil tankers, container ships, and others, in the marine environment have garnered significant attention. Underwater explosions, as an extreme and complex physical phenomenon, can cause severe damage to these structures. Gaining a deep understanding of the damage mechanisms of underwater explosions on ship structures and assessing their potential consequences are of great significance for ensuring the safety of maritime operations, optimizing structural design, and enhancing the explosion resistance of structures. After the explosion of underwater weapons, the explosion shock wave load and the bubble pulsating load in the water are mainly generated to damage the structure (Zhang et al., 2012; Achor et al., 2022; Henchie et al., 2014; Rajendran and Lee, 2008; Wu et al., 2022). Cole (1948) conducted a comprehensive analysis and extensive research on the physical laws of underwater explosions, based on a large number of underwater explosion experiments. Further, the propagation process of underwater explosion shock waves was analyzed, and the pulsation and movement patterns of underwater bubbles were summarized. In addition, Cole had considerable insights into the reflection and diffraction of underwater explosion shock waves as well as underwater testing systems, which provide significant reference for the research on underwater explosions. Jones (2011) studied the inelastic deformation behavior of various structures under large dynamic, impact and blast loads, and carried out in-depth analysis and research on the

Article Highlights

- Three types of damage modes of multi-cabin structure (MCS) were defined, and occurring conditions of these three damage modes were determined.
- Damage effects of different MCS surfaces were compared under dual-point and single-point explosion with the same total charge, and the damage mechanisms were revealed.
- A damage factor F^* was proposed to determine the damage mode of the MCS under the simultaneous explosion of two explosives. F^* reflects the influence of multi factors including the explosive mass, the explosion distance, and the spacing between explosives, et al.

✉ Jinxiang Wang
wjx@njust.edu.cn

[1] National Key Laboratory of Transient Physics, Nanjing University of Science and Technology, Nanjing 210094, China

impacts of lateral shear, rotational inertia, finite displacement, and material dynamic performance. The law of scale is discussed, which is important for applying the results of small-scale tests to predict the dynamic behavior of full-scale prototypes. Wu et al. (2020) proposed a novel numerical method for investigating underwater cavitation. This method demonstrates superior accuracy in simulating the propagation of underwater explosive shock waves compared to existing acoustic-structure coupling approaches. Zhang et al (2023) proposed a new theory of bubble dynamics in latest study. The effects of boundaries, bubble interactions, ambient flow field, gravity, bubble migration, fluid compressibility, viscosity and surface tension are considered, different classical bubble theories are unified, and the interaction of complex multi-period bubbles with a wide range of energies and phase differences is simulated.

The near-field underwater explosion of explosives can cause serious damage to ships (Costanzo, 2012; Gao et al., 2023; He et al., 2023). Scholars often use partial or simplified models to study ship damage. In the study of ship damage, ship hull simplified models (He et al., 2020; Zhang et al., 2020), multi-layer structure (Jin et al., 2019; Qin et al., 2022), and the reinforced plate structure (Jen and Tai, 2010; Truong et al., 2021) are commonly used. Wu et al. (2021) investigated the strongly nonlinear interaction between bubbles and elastoplastic plates, thereby addressing a research gap in this field. Chung and Nurick (2005) conducted a study on the response of stiffened plates with different stiffening methods under uniform explosive loading and local explosive loading, and compared the test results with simulation results. Bonorchis and Nurick (2010) has shown that different weld types have a certain effect on the response of the stiffened plate under blast loads. Numerical simulation is good for predicting the large deformation of welded stiffened plate, but further research is needed in the case of tensile tear failure. Zhou et al. (2021) analyzed the response of the ship box structure under the combined action of surface waves and underwater explosions, arguing that the synergistic effect of waves and underwater explosions would exacerbate the damage to the ship box structure, and the combined effect of the second bubble pulsation and sinking waves would cause greater deformation to the hull girder. Li et al. (2021a) thoroughly examined the influence of structural and fluid damping factors on the dynamic response of a ship's hull girder with a uniform cross-section, particularly when it is subjected to a direct explosion beneath the mid-span. Incorporating the damping effects, a refined theoretical model was established to accurately predict the fully elastic and elasto-plastic responses of the hull girder under the combined influence of explosion shock waves and bubble pulsations. Li et al. (2021b) has studied the response of three types of cabin structures with non-reinforced, single-reinforced, and double-reinforced plates under the action of internal explosion loads, and analyzed the effects of internal explosion wave characteristics, shock isolation distance, and the position of reinforcement ribs on the deflection and failure mode of the reinforced plates.

In modern local combat, underwater weapons often attack ships in groups. Currently, the research on the effects of multi underwater explosion on ship structures is still quite limited. In this situation, further exploring the damage effect of multi underwater explosion on ships is of crucial importance for advancing the research on ship protection capabilities. This study conducted a near-field underwater explosion experiment on a simplified multi-cabin structure (MCS). Under the action of near-field underwater explosion, MCS exhibited surface tensile tearing damage and irreversible plastic deformation. Using finite element simulation software, the experimental environment was replicated. The results indicated that the finite element software can significantly accurately simulate the damage caused by near-field underwater explosion on the MCS. Furthermore, this study identifies three characteristic dynamic damage modes for multi-cabin structures: large plastic deformation of the primary layer, sequential first-layer tearing combined with secondary-layer plastic deformation, and bilayer tensile tearing. A novel damage quantification metric F^* was developed based on these damage patterns, enabling accurate prediction of structural damage effects under dual-point explosion scenarios. The established damage modes and quantification methodology provide a groundbreaking analytical framework for investigating the destructive impacts of repeated underwater explosions on naval hull structures, significantly addressing the research gap in multi-explosion synergistic assessment.

2 Experimental investigation

2.1 Multi-cabin structure (MCS) design

Considering that it would be extremely expensive to design and build a complete warship structure model, in the case of near-field damage to a warship, the localized structures are often subjected to explosion. Most of the local structures at the bottom of a warship are multi-cabin structures. Therefore, study adopted a simplified multi-cabin structure for experiment. The outer shape of MCS model is a cube with dimensions of 1 180 mm × 1 180 mm × 1 180 mm (length, width, and height). Inside MCS, it is divided into 27 small hexahedral cabins arranged in a 3 × 3 × 3 grid (length, width, and height directions) by small square plates with dimensions of approximately 400 mm × 400 mm, which are connected together by wire welding. The thickness of the flat plate on the cabin surfaces and the outer surface of the MCS is 7 mm. The material of all the flat plates in MCS is Q235 steel. Q235 is a type of steel alloy

grade in China, which contains Mn, Si, S, and P. The density of Q235 steel is 7.83 kg/m^3, and the yield strength of heat-treated Q234 steel may reach up to 325 MPa. The elastic modulus of Q235 steel is 200 GPa, and its Poisson's ratio is 0.3. Since the entire MCS was sealed, during underwater explosion testing, the buoyancy acting on MCS is greater than its own weight, therefore, additional ballast needs to be added to sink MCS underwater. The concrete counterweight was connected to MCS by thick rope binding and welding, as shown in Figure 1. The welding method between the concrete counterweight and MCS was spot welding, which will not affect the test results.



Figure 1 Overall diagram of the MCS

2.2 Experimental conditions

The experiment was conducted in an explosion pool with a surface diameter of approximately 7 m and a depth of approximately 3.5 m. The MCS was subjected to near-field underwater explosion damage using 1 080 g TNT explosive. The dimensions and density of TNT are shown in Table 1. The purpose of this experiment was to study the damage effect of MCS subjected to near-field underwater explosion, and the results of the experiment will provide support for the following numerical study. Determining the power of explosives is the basis for conducting research on the destructive power of underwater explosion. Therefore, a static underwater explosion test was conducted using TNT explosive of the same quality and from the same batch, and an underwater free-field sensor was used to measure the pressure of the explosion shock wave. Two PCB-W138A05 underwater free-field pressure sensors were arranged at the same depth as the explosive, with distances of 2.5 meters and 3 meters from the explosive respectively.

Table 1 Explosive parameters

Explosive	Diameter (mm)	Height (mm)	Mass (g)	Density (g/cm^3)
TNT	90	114	1 080	1.49

In order to fix the position of the explosives, a positioning rod was spot-welded above the bulkhead wall on the upper surface, and the explosives were fixed on the positioning rod through a steel cable. The explosive was placed on the upper surface of the MCS, and the distance between the bottom of MCS and the upper surface of the box was 60 mm. The position of the positioning rod and the explosive on the upper surface of the box are shown in Figure 2. During the lifting process, the MCS was gradually lowered into the center bottom of the pool.

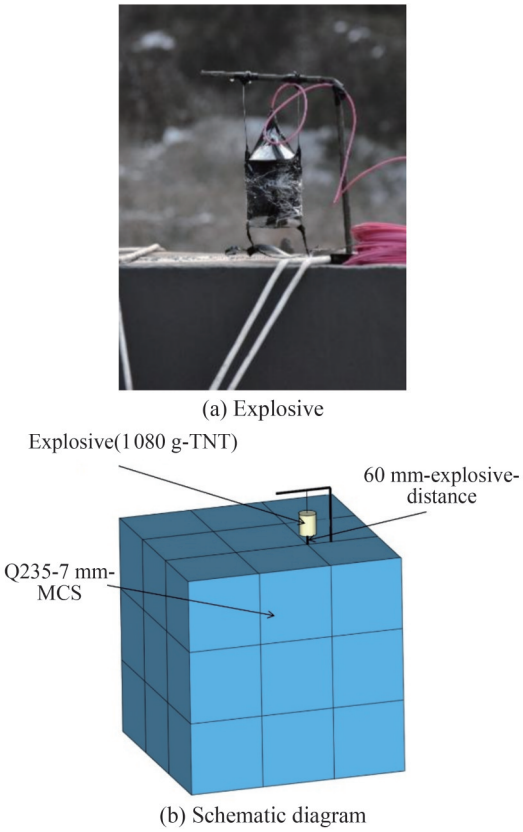


Figure 2 Explosive charge placement location

3 Numerical simulation

Due to the limitation of test and measurement conditions, the damage mechanism of underwater explosion on MCS is not clear. In order to conduct further study, numerical simulation was used to simulate the damage process of MCS. When it comes to the study of the damage effect of underwater explosions on structures, LS-DYNA has become the first choice of most scholars due to its high precision, high efficiency, high applicability, and strong post-processing capabilities (Chen et al., 2023; Tian et al., 2023; Zhou et al., 2024).

3.1 Euler-Lagrange algorithm theory

The Euler and Lagrangian methods are usually used to calculate the damage to structures by the near-field under-

water explosion shock wave. In the Euler method, the computational mesh is consolidated in the spatial coordinates, and simulation mesh remains unchanged during the deformation of the object. Thus, the distortion of the medium can be completely handled. However, the motion interface identification requires the introduction of an extremely complex mathematical mapping, which can cause severe errors. In the Lagrangian method, the simulation grid is fixed on the object and moves with the object; in addition, the grid point in physical space-time always coincides with the material point during the deformation of the object, and no relative motion appears. In some cases, however, the mesh deformation might be extremely large to fail the calculation. The arbitrary Lagrangian-Euler (ALE) method organically combines the Euler and Lagrangian methods to exploit the advantages of both methods. The ALE method is usually used for the calculation of force deformation of solids in the flow field.

The control equation of the ALE method is expressed by the mass conservation, momentum, and energy conservation equations, as follows:

$$\frac{\partial \rho_{\mathrm{F}}}{\partial t} = -\rho_{\mathrm{F}} \frac{\partial v_i}{\partial x_i} - W_i \frac{\partial \rho_{\mathrm{F}}}{\partial x_i} \tag{1}$$

$$v \frac{\partial v_i}{\partial t} = \sigma_{ij} + \rho_{\mathrm{F}} b_i - \rho_{\mathrm{F}} W_i \frac{\partial v_i}{\partial x_j} \tag{2}$$

$$\rho_{\mathrm{F}} \frac{\partial E}{\partial t} = \sigma_{ij} v_{ij} + \rho_{\mathrm{F}} b_i v_i - \rho_{\mathrm{F}} W_i \frac{\partial E}{\partial x_j} \tag{3}$$

The enhanced form of the Newtonian fluid flow problem, which controls the fixed domain, consists of a control equation and corresponding initial boundary conditions. The equation that governs the fluid problem is the ALE description of the N-S equation, where ρ_{F} is the density of the fluid and w_i is the difference between the velocity v of matter and grid velocity u, so-called the relative velocity. The derivation of Euler's equation is based on the assumption that the velocity of the reference configuration is zero and relative velocity of the matter and reference configuration is the velocity of matter. The convection term in the momentum conservation equation is used to calculate the amount of material transported through the grid.

The structural domain is typically described using the Lagrangian framework, and its governing equations is:

$$\rho_{\mathrm{s}} \frac{\partial^2 \boldsymbol{d}_s}{\partial t^2} = \nabla \cdot \boldsymbol{\sigma}_s + \boldsymbol{f}_s \tag{4}$$

where ρ_{s} is structural density, $\boldsymbol{d}_{\mathrm{s}}$ is structural displacement vector, $\boldsymbol{\sigma}_{\mathrm{s}}$ is structural stress tensor, $\boldsymbol{f}_{\mathrm{s}}$ is external load vector.

The ALE equation can be solved using the fully-coupled equation for computational fluid dynamics or operator separation algorithm; in addition, the calculation at each time step is divided into two stages. The Lagrange process is performed first, where the grid moves with matter. In this process, the velocity and amount of internal energy changes caused by external forces are calculated, and the equilibrium equation is expressed as

$$\rho \frac{\partial v_i}{\partial t} = \sigma_{ij} + \rho b_i \tag{5}$$

$$\rho \frac{\partial E}{\partial t} = \sigma_{ij} v_{ij} + \rho b_i v_i \tag{6}$$

When calculating the convection term, the mass transport, internal energy, and momentum across the element boundary are calculated, which can be considered as the displacement mesh of the Lagrange process remapping back to its initial position or arbitrary position.

Euler's algorithm requires a stable time step $\mathrm{d}t < \mathrm{d}x/(c + u)$, where $\mathrm{d}x$ is the element feature length, c is the velocity of material sound, and u is the particle velocity.

For solid substances, the velocity of material sound can be expressed as

$$c^2 = \frac{\frac{4}{3}G + k}{\rho_0} \tag{7}$$

$$k = \rho_0 \frac{\partial P}{\partial \rho} + \frac{P}{\rho} \frac{\partial P}{\partial e} \tag{8}$$

where ρ is the material density, G is the shear modulus, and P is the equation of state pressure. For fluid matter, $k = \rho_0 \times c^2$, where ρ_0 is the mass density and c is the speed of sound. Fluid substances ignore their viscosity when calculating the speed of sound.

The ALE mesh discretization method commonly employs the spring analogy method and Laplacian smoothing. In the spring analogy approach, the edges of the mesh are treated as virtual springs, and the mesh node positions are iteratively adjusted by achieving equilibrium of nodal forces to optimize the grid topology. The equation is expressed as

$$\sum_{j \in \mathcal{N}(i)} k_{ij} \left(\boldsymbol{x}_j - \boldsymbol{x}_i \right) = \boldsymbol{0} \tag{9}$$

where k_{ij} is the stiffness coefficient of the edge between nodes i and j, and $N(i)$ is the set of nodes adjacent to node i.

In Laplacian smoothing, the mesh motion is governed by a diffusion equation. The equation is expressed as

$$\nabla \cdot (k \nabla \boldsymbol{w}) = \boldsymbol{0} \tag{10}$$

where k is the diffusion coefficient, which can be locally adjusted to accommodate deformation requirements.

The ALE discretization of the governing equations is primarily divided into spatial discretization and temporal discretization. In spatial discretization, the fluid domain is partitioned into moving control volumes, and the integral form of the conservation equations is applied as follows

$$\frac{\mathrm{d}}{\mathrm{d}t}\int_{V(t)}\rho_f u_f \mathrm{d}V + \oint_{\partial V(t)}\rho_f u_f\left(u_f - w\right)\cdot n\mathrm{d}S = \int_{V(t)}\left(\nabla\cdot\sigma_f + f_b\right)\mathrm{d}V \tag{11}$$

The flux terms are corrected using the mesh velocity $\boldsymbol{w}$.

The temporal discretization employs the following implicit time integration approach to handle time derivatives on moving meshes.

$$\frac{\partial \boldsymbol{u}_f}{\partial t} \approx \frac{\boldsymbol{u}_f^{n+1} - \boldsymbol{u}_f^{n}}{\Delta t} + \boldsymbol{w}\cdot\nabla\boldsymbol{u}_f^{n+\theta}\left(\theta\in[0,1]\right) \tag{12}$$

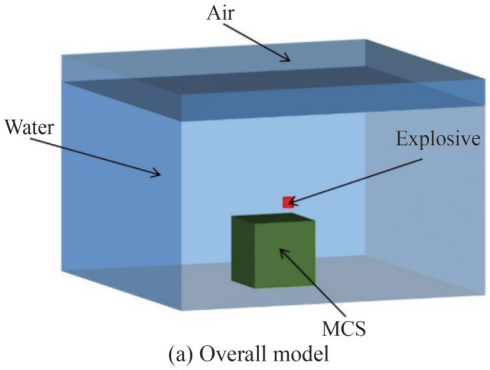
On the fluid-structure interface, the kinematic compatibility equation and the dynamic equilibrium equation must be satisfied as

$$\boldsymbol{u}_f = \frac{\partial d_s}{\partial t} \tag{13}$$

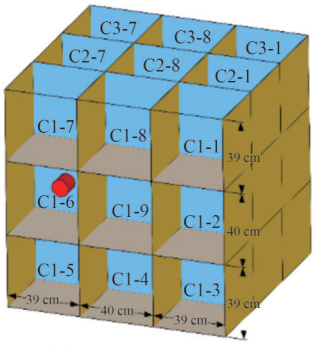
$$\boldsymbol{\sigma}_f\cdot\boldsymbol{n}_f = \boldsymbol{\sigma}_s\cdot\boldsymbol{n}_s \tag{14}$$

3.2 Numerical simulation model

Based on the test conditions introduced in section 1.2, a numerical simulation model was established. Due to the asymmetry of the simulation model, the full-sized model was established for numerical simulation. The numerical simulation model consists of four parts: air, water, explosive, and a MCS. In this model, the air, water, and explosive are modeled as Eulerian grids, while the multi-cabin box structure is modeled as Lagrangian grids. Euler grids are coupled with Lagrangian grids by the *CONSTRAINED_LAGRANGE_IN_SOLID keyword. Since the MCS is composed of square flat plates, shell elements are used to enhance computational efficiency. The size of the Eulerian domain is 8 m × 8 m × 4 m, and the size of the MCS is 1.18 m × 1.18 m × 1.18 m. Local refinement method is employed for mesh generation, with a mesh size of 1cm in the refined regions. Non-reflecting boundary conditions are imposed on the Eulerian domain using the *BOUNDARY_NON_REFLECTING keyword. To maintain consistency with experimental observations, the velocity component in the Y-direction at the bottom boundary of the computational model was constrained. Both explosive and the air are filled in the Eulerian domain using the *INITIAL_VOLUME_FRACTION_GEOMETRY keyword. The dimensions of the explosive are 9 cm × 9 cm × 9 cm, and the size of the air on the upper surface of the Eulerian domain is 6 m × 6 m × 0.5 m. Since the MCS is sealed, it is filled with air of size 1.18 m × 1.18 m × 1.18 m. To simulate the experimental conditions, all faces of the Eulerian domain are set as fixed boundary conditions, and the bottom surface of the MCS is also fixed. The numerical simulation model is shown in Figure 3(a). The cabins are numbered using the CX-Y format. Here, X (ranging from 1–3) represents the cabin layer number based on proximity to the explosive, while Y (ranging from 1–9) denotes the individual cabin number within each layer, as shown in Figure 3(b). PX-Y denotes the primary blast-facing surface number within the CX-Y cabin.



(a) Overall model



(b) Cabin number of the MCS

Figure 3 Numerical simulation model of test conditions

3.3 Material parameters

In LS-DYNA, there are various constitutive models and equations of state for materials that can be selected and used. For water and air, the *MAT_NULL constitutive model and the *EOS_GRUNEISEN equation of state are generally used. The general expression for the GRUNEISEN equation of state is:

$$\begin{cases} p = \dfrac{\rho_0 c_0^{\,2}\mu\left[1+\left(1-\dfrac{\gamma_0}{2}\right)\mu - \dfrac{a}{2}\mu^2\right]}{\left[1-(S_1-1)\mu - S_2\dfrac{\mu^2}{\mu+1} - S_3\dfrac{\mu^3}{(\mu+1)^2}\right]^2} + \left(\gamma_0 + a\mu\right)e, & \mu \geqslant 0 \\ p = p_0 c_0\mu + \left(\gamma_0 + a\mu\right)e, & \mu < 0 \end{cases} \tag{15}$$

where c_0 is the speed of sound; μ is the degree of compression, $\mu = \rho/\rho_0 - 1$, when $\mu > 0$, the water is in the compressed state, and when the $\mu < 0$ is in the expansion state; γ_0 is the Mie-Grüneisen coefficient; a is the volume correction factor; S_1, S_2 and S_3 are the experimental fitting coefficients. e is the specific internal energy per unit volume. The specific parameters of the equations of state of water and air are shown in Tables 2 and 3.

Table 2 Equation of state parameters for water *EOS_GRUNEISEN

ρ_0/(g·cm^{-3})	c_0(m·s^{-1})	S_1	S_2	S_3	γ_0	a
1.0	1480	2.56	−1.986	0.2268	0.4934	0.07

Table 3 Equation of state parameters for air *EOS_GRUNEISEN

ρ_0/(g·cm^{-3})	c_0(m·s^{-1})	S_1	S_2	S_3	γ_0	a
0.0125	344	0	0	0	1.4	0

Explosives are typically described using the *MAT_HIGH_EXPLOSIVE_BURN constitutive model and the *EOS_JWL (Jones–Wilkins–Lee) equation of state (Zhao et al., 2020). The JWL equation of state defines pressure as a function of the relative volume V and the internal energy e per unit initial configuration volume, and the expression is given in Equation (9):

$$p = C_1\left(1 - \frac{\omega}{R_1 V}\right)e^{-R_1 V} + C_2\left(1 - \frac{\omega}{R_2 V}\right)e^{-R_2 V} + \frac{\omega \rho e}{V} \quad (16)$$

where p is the pressure; V is the relative volume; ρ is the initial density of explosives; e is the specific internal energy per unit mass; ω, C_1, C_2, R_1, R_2 are constants that characterize the characteristics of explosives. The material parameters of TNT explosive are shown in Table 4.

Table 4 EOS_JWL equation of state parameters for explosives

ρ_0/(g·cm^{-3})	e (MJ·kg^{-1})	C_1 (GPa)	C_2 (GPa)	R_1	R_2	ω
1.49	4.19	371.2	3.231	4.15	0.95	0.30

Q235 carbon steel is described using the *MAT_JOHNSON_COOK constitutive model (Zhou et al., 2019). The relation of stress and strain is defined by the J-C constitutive model, in which the influence of strain rate effects is considered. The functional expression is (ignoring temperature effects):

$$\sigma_{eq} = \left(A + B\varepsilon_{eq}^{n}\right)\left(1 + C\ln\dot{\varepsilon}_{eq}^{*}\right) \quad (17)$$

where σ is stress; A is the yield strength of the material at the reference strain rate; B and n are the strain strengthening coefficients; C is the strain rate sensitivity coefficient; σ_{eq} is the equivalent stress; ε_{eq} is the equivalent plastic strain; $\dot{\varepsilon}_{eq}^{*}$ is the dimensionless equivalent plastic strain rate, $\dot{\varepsilon}_{eq}^{*} = \dot{\varepsilon}_{eq}/\dot{\varepsilon}_0$, and $\dot{\varepsilon}_0$ is the reference strain rate. The Johnson-Cook failure model is suitable for describing the failure of metals at high strain rates, and the expression is (ignoring temperature effects):

$$\varepsilon_f = D_1 + D_2 e^{\left(D_3\sigma^{*}\right)} \cdot \left(1 + D_4 \ln\dot{\varepsilon}_{eq}^{*}\right) \quad (18)$$

For Q235 carbon steel material, the J-C parameters are shown in Table 5.

Table 5 Q235 carbon steel J-C parameters

ρ_0(g·cm^{-3})	A	B	n	c	D_1	D_2	D_3	D_4
7.83	3.25	2.20	0.21	0.022	−43.408	44.608	−0.016	0.0145

4 Analysis and discussing

4.1 Numerical simulation verification

4.1.1 Verification of the shock wave pressure

During the propagation of underwater explosion shock waves, the pressure first rapidly increases to a peak value and then decreases exponentially. As the distance between the measuring point and the explosion source increases, the peak pressure of the shock wave decreases rapidly. Figure 4 shows the comparison of pressure history curve of the shock wave pressure between the numerical and experimental results. At the 2m measurement point, the peak pressure of the shock wave from the experiment was 17.60 MP, while the peak shock wave pressure from the numerical simulation was 17.82 MPa, with an error of 1.2%. At the 2.5 m measurement point, the peak pressure from the experiment was 13.52 MPa, while the peak shock wave pressure from the numerical simulation was 13.83 MPa, with an error of 2.3%. The difference in the peak pressure of the shock wave measured between the numerical simulation and the experiment is very small. Moreover, the downward trend of the shock wave pressure is largely consistent. Further observation reveals that the area enclosed by the historical curve and the time axis is very similar, indicating that the impulse of the shock wave generated by the numerical simulation is close to that of the experiment. The pressure peak and impulse of the shock wave are the key parameters to evaluate the damage effect of the shock wave to the structure. Therefore, numerical simulation has high effectiveness in simulating the damage of the underwater explosion shock waves caused on the structures. In numerical simulations, there may be fluctuation in the shockwave descending curve, which are caused by numerical oscillation.

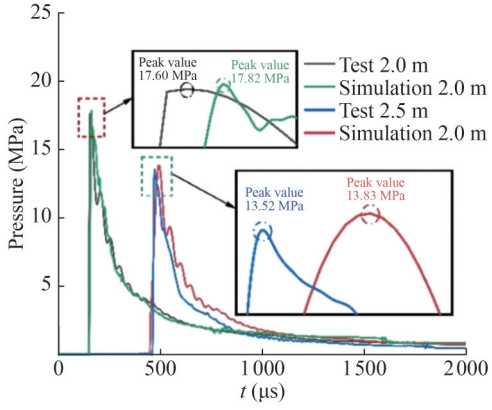


Figure 4 Historical curve of shock wave pressure

4.1.2 Verification of damage results

Figure 5 shows the damage results of the MCS in both experimental and numerical simulations under the test conditions. The four cabin surfaces on the MCS that were close to the explosive all suffered very severe tensile tearing damage, and there was obvious bending deformation and inward denting on the outer panel of the cabin. The vertical plate between the cabins has undergone bending deformation and been bent to one side. As shown in Figures 5(i) and 5(j), the partial tearing occurs at the upper end of the outer plate of the middle cabin. In Figures 5(k) and 5(l), P1-1 to P1-5 in Figure 5(k) have also suffered varying degrees of damage and deformation after being subjected to the shock wave of the explosive, mainly manifesting as plastic deflection deformation caused by indentation. Figures 5(m) and 5(n) show the damage effect of the MCS on the non-explosive surfaces. Both the test and the numerical simulation produced different degrees of plastic deflection on the non-explosive surfaces. This is because the shock wave has the characteristic of diffraction, and it can continue to propagate around the edges of obstacles after encountering them. When the shock wave propagates through the side of the MCS, it exerts pressure on the surface and causes damage effects. Figure 5 shows a high degree of consistency between numerical simulation and experimental results in terms of the damage mode and effect on the MCS. This consistency indicates that the numerical simulation model, algorithm, and material parameters can accurately predict the damage mode and effect of underwater explosion shock waves on MCS.

4.2 Dynamic response of MCS

Figure 6 shows the pressure contour plot of the shock wave during its propagation in water. The initial shock wave front generated by the explosion was nearly spherical rather than perfectly spherical due to the explosive's cylindrical rather than spherical shape. After the shock wave had continued to propagate outwards, the shape difference gradually disappeared, and eventually the distribution of the shock wave could be regarded as a spherical wave. Under the action of shock waves, the MCS undergoes bending deformation, which causes the outer plates to push the surrounding water, resulting in the generation of shock waves in the water due to the pushing effect of the plates. When the shock wave propagates to the edge of the MCS, the shock wave front is obviously curved. After that the shock wave will diffract around the obstacle. When the shock wave diffracts, the pressure at the wave front is less than that of the shock wave front without diffraction. At the edge of the MCS, the curvature radius of the shock wave front is relatively small; along the direction of the wave front, the curvature radius rapidly increases and maintains its maximum value; and when approaching the other side of the structural edge, the curvature radius decreases rapidly again.

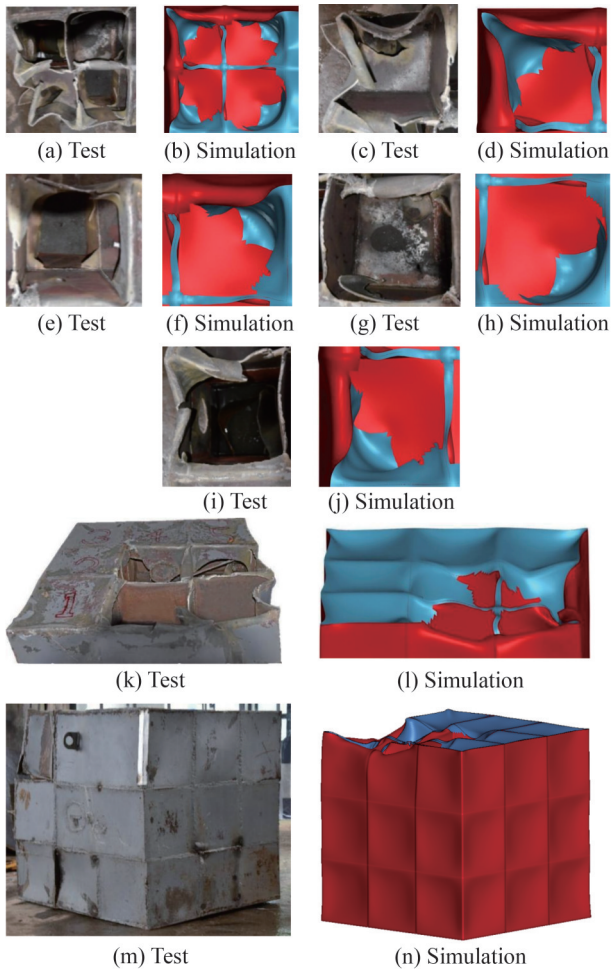


Figure 5 Comparison of the damage effect between the test and the simulation

Figure 7 illustrates the plastic deformation process of a MCS under the influence of underwater explosion shock waves. It can be observed that after the detonation of the explosive, the shock wave propagates outwards and interacts with the upper surface of the MCS. When t = 0.05 ms,

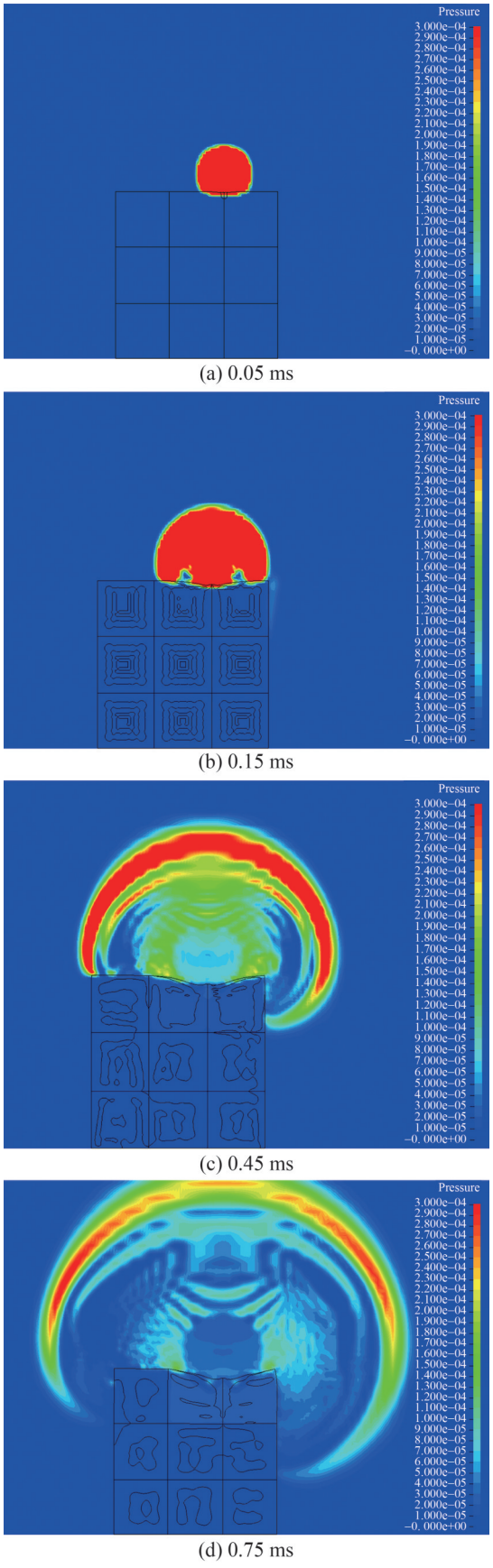


Figure 6 Cloud diagram of the shock wave propagation process

the MCS begins to undergo plastic deformation, with the area closest to the explosive being the first to deform. At t = 0.35 ms, the MCS reaches its plastic deformation limit, and the upper surface experiences tensile tearing failure. The torn elements occur on both sides of the vertical partitions, exhibiting a certain symmetry, and gradually spread outwards. The cracks meet in the middle, forming a larger tear. At t = 0.9 ms, the vertical plates at the edges of the MCS begin to curl inward due to the downward concave deformation of the upper surface under the action of the shock wave, which transfers the force to the edges and exerts a downward force on the vertical plates. It is worth mentioning that at t = 2.75 ms, from the tear on the upper surface, it can observe a certain degree of plastic deformation on the horizontal plate of the second cabin. Different levels of damage also appeared on the horizontal plate of the second cabin in the experiment, indicating that numerical simulation can effectively simulate the damage process of the MCS. However, due to the low welding strength of the test specimen, the horizontal plate of the test cabin suffered more severe damage. At t = 4.40 ms, the tear on the upper surface of the MCS reaches its maximum size, and no further severe plastic deformation or damage occurs, only elastic oscillation is present.

For P1-1 to P1-5, the final deformation deflection curve is plotted in Figure 8. The plastic deflection deformation of P1-1 and P1-5 is the most severe, while that of P1-2 and P1-4 is moderate, and the plastic deflection deformation of P1-3 is the smallest. This is because the closer to the explosion source, the greater the shock wave pressure and impulse received, resulting in a higher degree of damage. In the figure, the curves of P1-1 and P1-5, as well as P1-2 and P1-4, respectively represent the deflection curves of the centerlines in different directions that are symmetrical. Besides, the deformation of the plane is asymmetrical, mainly because the applied pressure is not loaded from the center front, but from the side. And there will be interaction between adjacent surfaces, resulting in different deformations. P1-1(5) and P1-2(4) are the same distance away from the explosive and receive the same amount of pressure from the explosion shock wave, but they exhibit different plastic deformations. P1-1(5) is the outer surface of the multi-cabin structure, while P1-2(4) is the middle surface. Although both receive shock waves of equal magnitude and direction, the force transmission between the adjacent plates is different, resulting in different deformation patterns.

Figure 9 shows the center deflection of the second-layer cabin surface, together with the density and pressure curves of the fluid in front of the plate. It can be observed that the center deflection of the plate mainly undergoes two stages: in the first stage, the plate rapidly experiences significant deformation, and in the second stage, the deformation intensifies based on the first stage. From the fluid

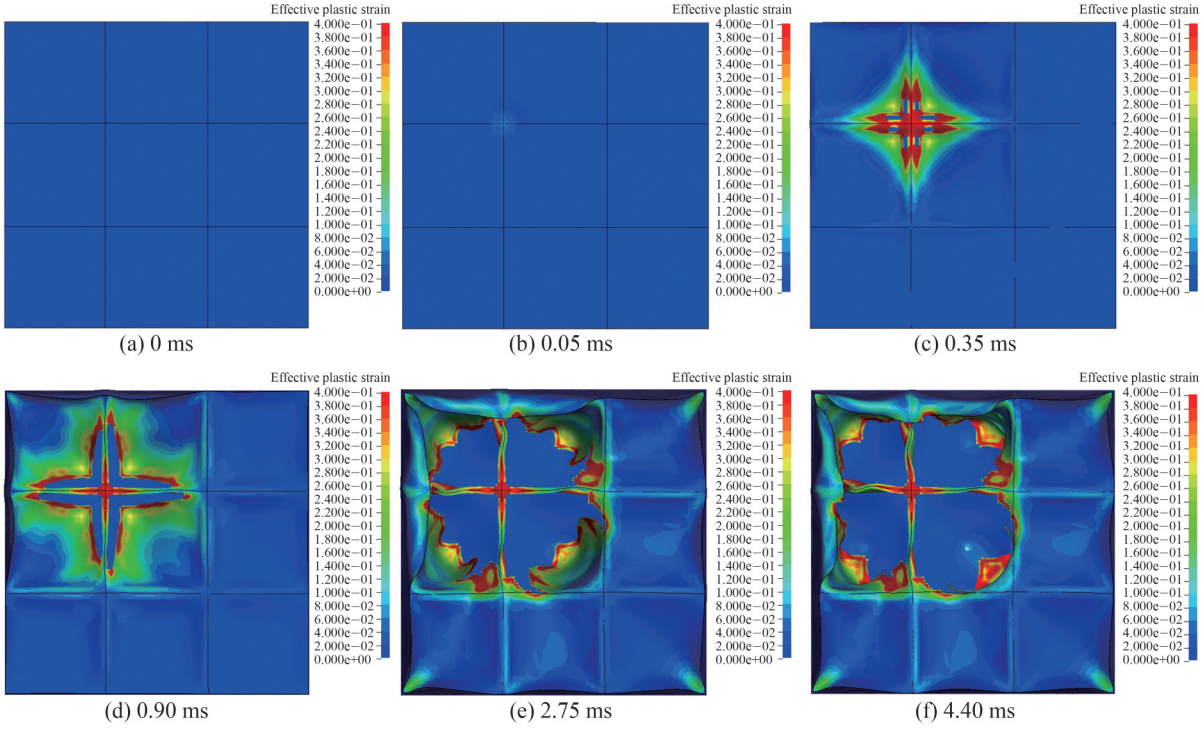


Figure 7 Effective plastic strain diagram of the MCS

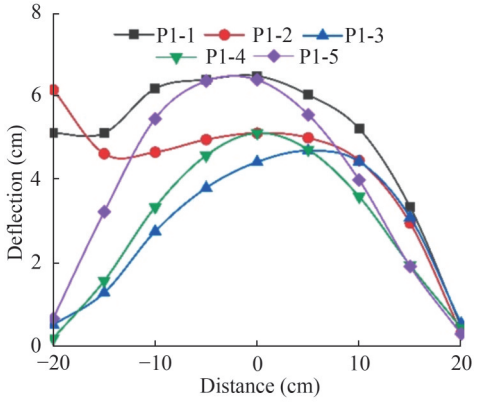


Figure 8 Deflection curve of the upper surface of the MCS

density curve and fluid pressure curve in the figure, it can be seen that the primary medium in front of the plate during the first stage of plate deformation is air. After the explosion shock wave interacts with the first layer of the plate, it undergoes transmission, and the pressure is transferred to the air in the cabin. And after the first layer of the plate ruptures, the air is compressed, resulting in a decrease in volume and an increase in pressure. The pressure within the air acts on the walls of the cabin. Although the peak pressure is not high, its duration is very long, resulting in significant plastic deformation of the plate. In the second stage of plate deformation, due to the rupture of the first layer of the plate, water enters the second cabin. Although the peak pressure of the water impact is greater than that of the air, the duration of its action is relatively short, and there are multiple instances of impact. Under the impact of water, the plate experienced further damage and deformation. Therefore, the plastic damage to the second cabin surface was formed by the combined damaging effects of multiple pressure stages. Other plates adjacent to the plate also have a certain influence on its deformation, but this process is too complex and will not be further discussed here.

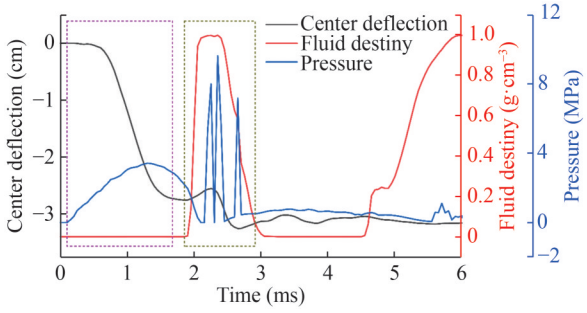


Figure 9 Deflection of the plate and the fluid density and pressure curve in front of the plate in the second layer cabin

Figure 10 shows the change in the pressure contour inside the cabin after the shock wave acts on it. When the shock wave reaches the upper surface plate of the first layer cabin, it undergoes transmission, propagating through the sequence of water-plate-air. When the wave enters the first layer cabin, it propagates from top to bottom and reflects after encountering the upper surface of the second layer cabin. The upper surface of the first layer cabin experiences tensile tearing

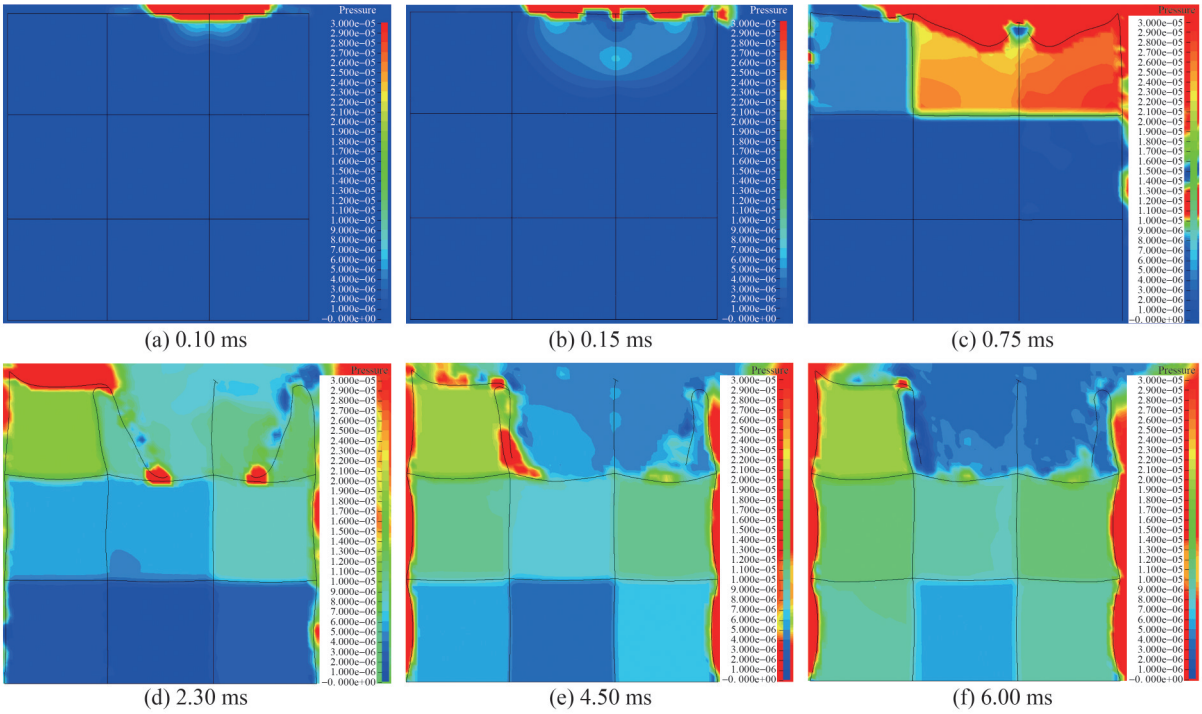


Figure 10 Pressure contour inside the cabin subjected to underwater explosion

and downward concave bending under the action of the shock wave. As it approaches the upper surface of the second layer cabin, a local high-pressure area is generated between the upper and lower plates. This pressure acts on the lower plate, causing it to bend and deform. Due to the diffraction effect of the shock wave, the outer surfaces around the MCS also undergo some deformation. The air inside generates a certain pressure under the deformation and compression of the cabin and the transmission of the shock wave, and then stabilizes. The middle cabin on the lower layer experiences minimal wall deformation and is least affected by the transmission of the shock wave, making it the area with the lowest pressure in the entire MCS.

The pressure time history curves of the Eulerian element at the center of each cabin are shown in Figure 11. Due to the symmetry of the entire model and the placement of the explosives, the pressure curves of C1-1 and C1-5, C1-2 and C1-4, C1-6 and C1-8 are nearly identical. Therefore, when discussing, the symmetrical cabin on the other side will be ignored. In Figure 11(a), the pressure inside C1-1 is greater than that of C1-2, which is consistent with the previous analysis because the deformation of C1-1 is larger than that of C1-2. It is noteworthy that the pressure inside C1-3 is lower than that of C1-1 but higher than that of C1-2, which is a very interesting phenomenon. This is because the diffraction phenomenon causes three surfaces of C1-3 to undergo significant deformation, while only two surfaces of C1-2 experience substantial deformation. Therefore, the internal air compression in C1-3 is more pronounced than that in C1-2. Air compression is a significant factor contributing to changes in the internal pressure of cabins. Due to the damage caused by the explosion shock wave, the internal Eulerian domain pressure curves of C1-6 to C1-9 differ from those of C1-1 to C1-5. The peak pressure is highest in C1-7, reaching 9.89 MPa, followed by C1-6 at 9.62 MPa, while C1-9 has the lowest peak pressure of only 5.36 MPa. Since cabins C2 and C3 did not suffer any breakage damage, the internal pressure changes in these cabins are similar to those in C1-1 to C1-5. Among the cabins located at the corners of each layer, Cabin 3 has the highest internal pressure, followed by Cabin 7, while Cabin 1 has the lowest internal pressure. It appears that there is a clear correlation between internal pressure changes in cabins and the relative position of the explosive. In cabins on the same layer, the internal pressure is higher when the cabin is farther away from the explosive. Cx-9, located at the center of each layer, experiences the smallest deformation of its surrounding walls and thus has the lowest internal pressure. The rate of internal pressure increase in C3 is significantly slower than that in C2 and C1.

4.3 Damage modes of MCS subjected to different explosion locations

Different explosive distances and shock wave positions result in distinct damage modes and deformations on MCS. To comprehensively evaluate the damage effects of explosives on MCS at different positions, an in-depth numerical simulation study was conducted using 1 080 g-TNT

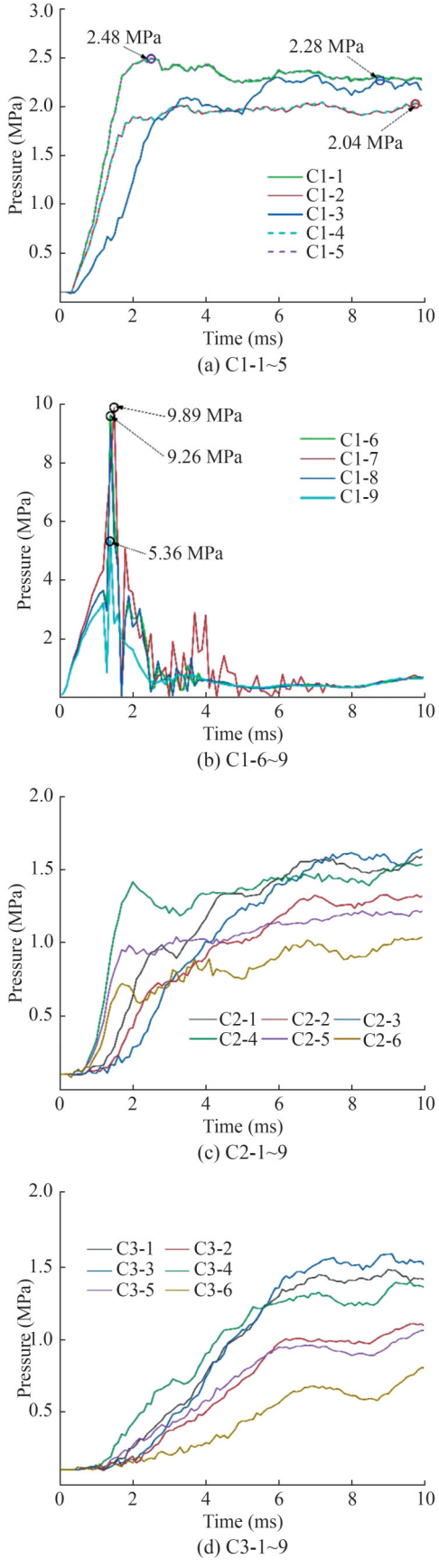


Figure 11 Eulerian domain pressure curve in the center of the cabin

explosives to investigate their impact on MCS from various orientations.

Damage mechanisms are analyzed with explosion distances spanning 0−25 cm, using 1 080 g-TNT detonated at central and corner positions on the centre cabin, respectively.

Based on the differences in damage effects, they are mainly categorized into two scenarios: tensile tearing failure and large plastic deformation. Meanwhile, considering the damage states of the first and second layers, there exist the following three damage modes:

I) The first layer experiences large plastic deformation;

II) The first layer exhibits tensile tearing failure, while the second layer experiences large plastic deformation;

III) Both the first and second layers suffer from tensile tearing failure.

The numerical simulation results of the three damage modes are shown in Figure 12.

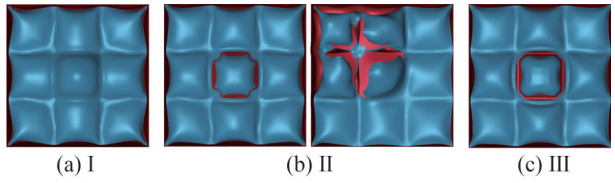


Figure 12 Three different damage modes of the MCS

The results have been meticulously classified into three different damage modes, with a damage criterion diagram subsequently constructed as shown in Figure 13.

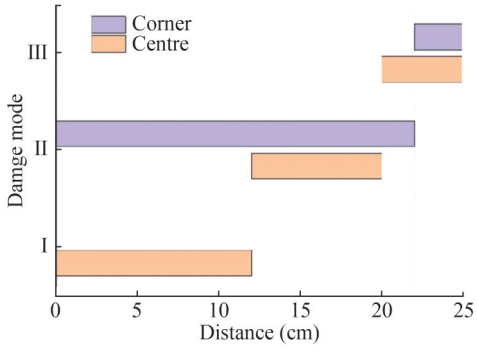


Figure 13 Damage criterion diagram

As clearly shown in Figure 3, the location of shock wave impact has a significant influence on the damage effects on the MCS. Specifically, when the shock wave directly acts on the central area of the plate (centre condition), the damage mode exhibits different characteristics as the distance between the explosive and the plate surface varies: within a distance range of 0 to 10 centimeters, it results in severe damage corresponding to Mode III; as the distance increases to 10 to 20 centimeters, the damage shifts to Mode II; and when the distance further expands to 20 to 25 centimeters, it produces milder damage corre-

sponding to Mode I. On the other hand, when the shock wave directly acts on the corner of the plate (corner condition), it primarily results in Mode II damage effects at a distance of 0 to 20 centimeters between the explosive and the plate surface; whereas when the distance is adjusted to 22 to 25 centimeters, Mode I damage effects are observed. In the "corner condition", Mode III damage effects were not observed. Compared to the "centre condition", the explosive in the "corner condition" is capable of producing Mode II damage effects on the MCS at farther distances. This demonstrates that the position of the shock wave's impact has a significant influence on the structural damage modes.

Through a thorough analysis of the effective plastic strain diagrams (as shown in Figure 14) for the central regions of the first and second layers under the centre condition, it can be observed that the second significant deformation of the first layer's center occurs almost simultaneously with the large-scale deformation of the second layer's center. This phenomenon strongly supports the inference that after the first plate experiences tensile tearing, the large fragment generated impact the second plate, triggering large-scale deformation in the second plate and ultimately leading to the occurrence of tensile tearing failure. This conclusion is further comprehensively and strongly corroborated after referencing and analyzing Figure 15. In contrast, under the corner condition, the first plate did not generate large fragments that impacted the second plate, thus no Mode III damage effects were observed. This contrast further highlights the significant influence of the shock wave's impact position and the interaction between the plates on the damage modes.

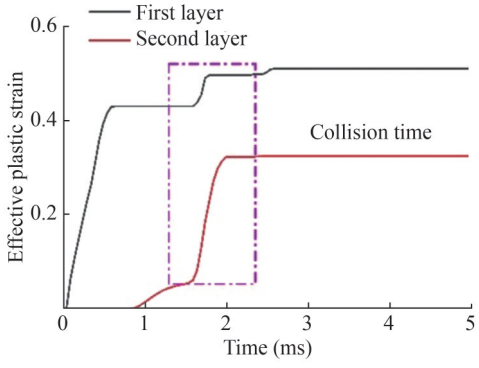


Figure 14 Effective plastic strain at the centers of the first and second plates

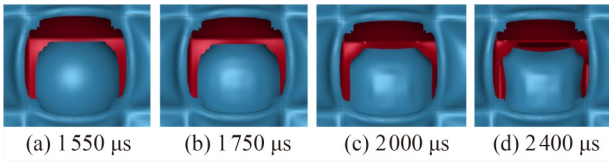


Figure 15 Deformation process diagram of the MCS under damage Mode III

4.4 Damage of MCS caused by two-point explosions

In previous research (Lin et al., 2021), it was found that the shock waves generated by the simultaneous detonation of multiple underwater explosives produce a superposition effect, resulting in a significant increase in pressure peaks compared to those generated by a single explosive. Within a certain range of positions, this superimposed pressure can be more than twice that produced by a single explosive. Due to the superposition effect of shock waves, the damage caused to structures by the simultaneous detonation of multiple explosives far exceeds that caused by a single explosive, and this effect is even better than the damage caused by the explosion of a single explosive with a mass equal to the total mass of multiple explosives.

4.4.1 Numerical simulation conditions

To further investigate the damage effects of simultaneous detonation of multiple underwater explosives on MCS, numerical simulation is employed for deeper research. TNT explosives of 1 080 g and 540 g are selected in numerical simulation. Figure 16 illustrates the schematic diagram of the explosive placement, and Table 6 lists the relevant parameters of different working conditions in detail.

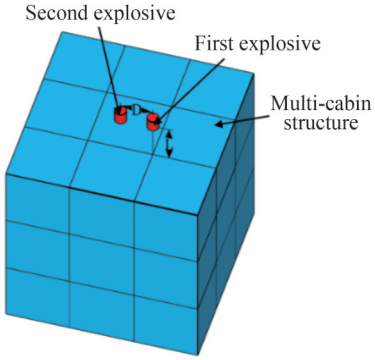


Figure16 Schematic diagram of the placement of explosives

4.4.2 Shock wave interaction process and MCS response results

Figure 17 illustrates the process of shock wave acting on the MCS under different working conditions. When the distance between two explosives is very close, the two shock waves generated by the explosion will intersect on the symmetrical plane, quickly merge into an ellipsoidal shock wave, and propagate outward in the medium. On the wave front of this ellipsoidal shock wave, the shock wave pressure on the symmetrical plane of the two explosives is greater than that of other places, and the width of the wave head is wider. This means that the shock wave in this part of the area has a longer action time and a larger impulse compared to other areas. Therefore, the shock wave in this part of the area has a more severe damage effect on the

Table 6 Parameters of underwater explosion under different working conditions

Working condition	The mass of a single explosive, W (g)	Number of explosives	Distance between explosives, D_E (cm)	The distance between the bottom of the explosive and the upper surface of the MCS, L (cm)
1	1 080	1	–	24
2	540	1	–	24
3	540	2	10	24
4	540	2	20	24
5	540	2	30	24
6	540	2	40	24

structure. As the distance between the explosives increases, the wave fronts of the two explosion shock waves will not form an ellipsoidal shock wave front after intersecting, but rather a union of two intersecting spherical surfaces. At this time, the damage mode caused by the explosion shock wave to the MCS is different from the previous one. Two individual shock waves will first act on the MCS, and then the superimposed shock wave will have a secondary effect on the structure, as shown in working conditions 5 and 6 in Figure 17.

The damage effects of underwater explosions on MCS under different working conditions are different, as shown in Figure 18. Compared to working condition-2, working condition-1 caused more severe damage effect. This is because, although the explosion distances are the same for both conditions, the mass of the explosive used in working condition-1 is twice that of working condition-2, resulting in a much larger explosion shock wave. Comparing working conditions 3 to 6, it can be seen that as the distance between the two explosives gradually increases, the damage effects on P1-9 undergo significant changes. Initially, it results in a larger breach; subsequently, it transitions to smaller tensile tearing; and ultimately, no tearing damage occurs. This series of changes indicates that as the spacing between the explosives increases, the overall damage effect on the MCS gradually weakens. Although P1-8 and P1-9 are symmetrically distributed on both sides of the explosive, the damage effects they experience are not the same. P1-8 only experiences significant plastic deformation, while P1-9 experiences destructive damage. This is because the outer plate of the MCS absorbs a large amount of energy during deformation, thereby reducing the damage effect on P1-8. When comparing working condition-1 with working condition-3–-6, it can be observed that in working condition-1, the deformation of P1-8–-9 is relatively small, whereas conversely, the deformation of P1-5–-6 is relatively significant. This phenomenon indicates that, when the total mass of explosives remains consistent, only the bulkhead surfaces located in the planar area between two explosives will suffer more severe damage, while those located on the outer sides of the explosives will experience relatively lesser damage.

To analyze the damage effects of single-point versus dual-point explosive charges on the MCS under identical total mass conditions, contour maps depicting the peak overpressure distribution on the MCS surface were generated, as illustrated in Figure 19. In working condition-1, the peak overpressure of the shock wave reaches 272 MPa. In contrast, working condition-3 to -6 exhibit values of 306 MPa, 345 MPa, 337 MPa, and 294 MPa, respectively. It is observed that compared to the shock wave peak overpressure produced by a single 1 080 g TNT charge, the simultaneous detonation of two 540 g TNT charges generates a shock wave with a higher maximum peak overpressure and a larger area of high-pressure distribution. Working condition-4 exhibited the most extensive high-pressure zone, reaching 627 cm^2. A comparative analysis of Figures 18 and 19 reveals that the enhanced damage inflicted on the MCS by the dual-point detonation is primarily attributable to its higher peak overpressure.

The comparison of the central deflection of P1 between working conditions-1 and -3 is shown in Figure 20. There are differences in the use of explosives between working conditions 1 and 3. Although the total mass of the explosives is the same for both conditions, the number of explosives is different. Compared to working condition-1, the relative position of the explosives to the MCS in working condition-3 is not symmetrical. This asymmetry produces a very obvious result: the deflection of each surface of P1 under the explosive shock load is different. Under these two working conditions, the plastic deformation exhibited by surfaces P1-1 to P1-7 shows a high degree of consistency. For surfaces P1-1 to P1-7, they are subjected to a larger single shock wave in working condition-1, while in working condition-3, they are subjected to two smaller shock waves with a very short interval. The damage effects produced by the two conditions are very close, although the mechanisms are different. This is because when the distance is sufficient, the superposition of explosion shock waves generated by two simultaneously detonated explosives of equal mass is similar to the shock wave generated by the explosion of a single explosive with double the

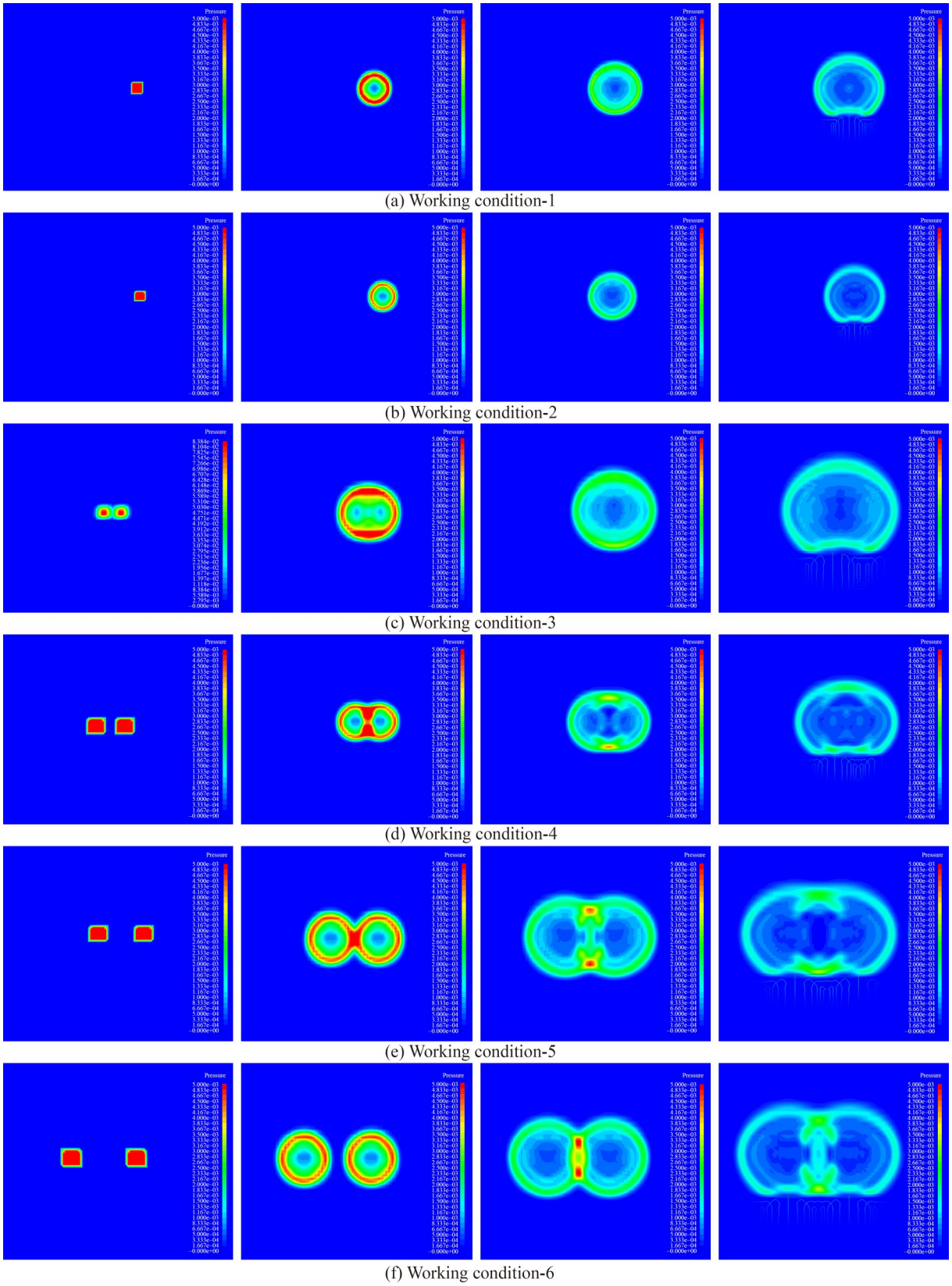


Figure 17 Diagram of shock wave propagation process

mass. For surfaces P1-8 and P1-9, the damage effects produced by the MCS under the two working conditions show distinctly different results. Compared to working condition 1, the plastic deformation deflection of P1-8 in working con-

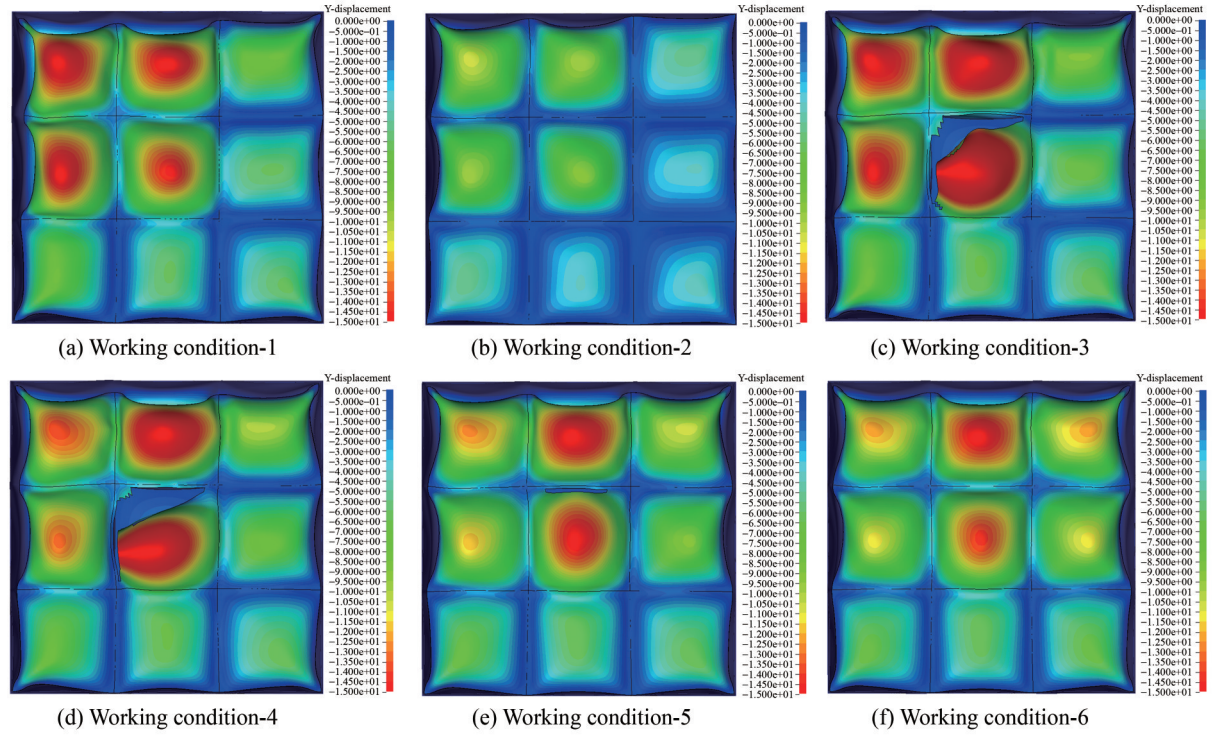


Figure 18 Contour diagram of deformation deflection of MCS under different working conditions

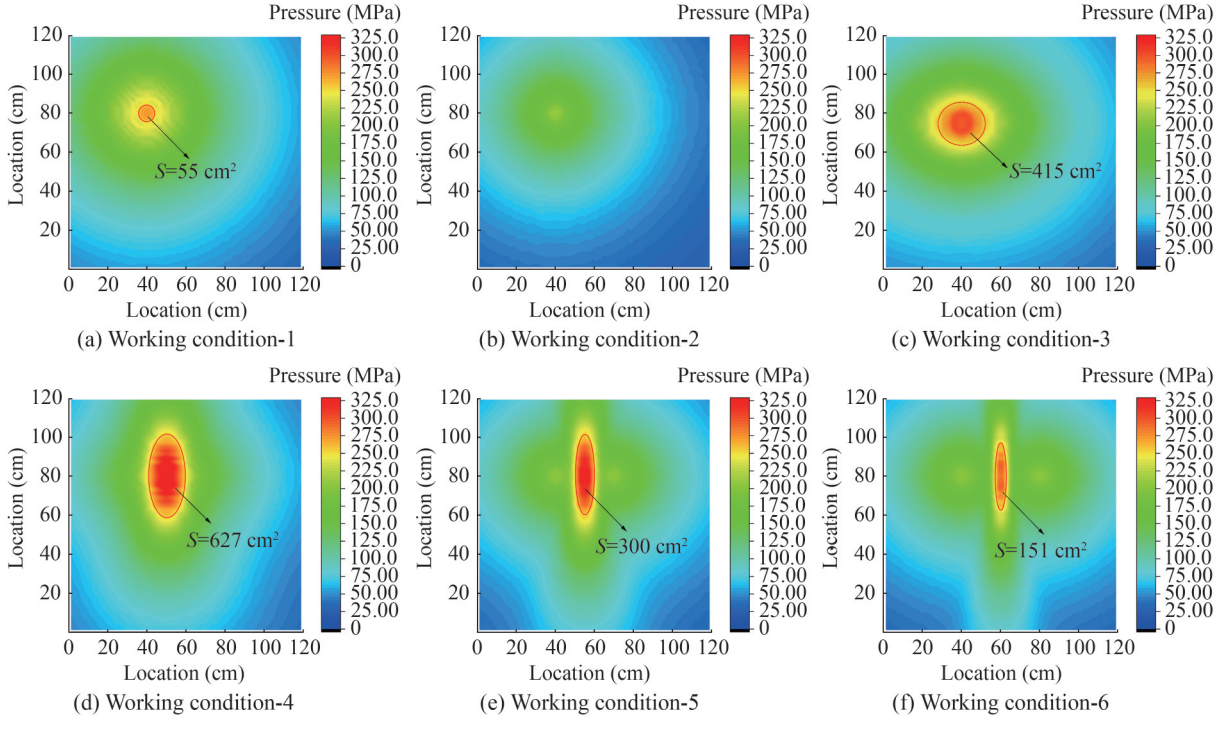


Figure 19 Peak overpressure contours on the MCS surface

dition 3 is much larger. P1-9 in working condition-3 suffers severe tearing and rupture damage, showing significant destruction, while in working condition 1, it only experiences large plastic deformation with relatively less damage. Under working condition-3, P1-9 is subjected to a larger shock wave pressure generated by the superposition of two explosion shock waves, which is much greater than the peak pressure of the explosion shock wave generated by a single explosive of the same mass in working condition 1. Therefore, the damage effect formed by P1-9 in working

condition-3 is more significant, and the degree of damage is more severe.

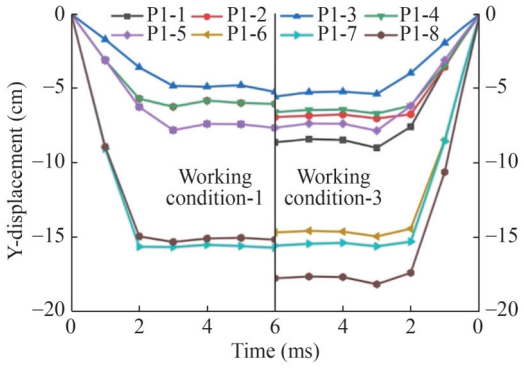


Figure 20 Comparison of the central deflection of P1-1–8 in working condition-1 and working condition-3

Figure 21 shows the equivalent plastic strain curve at the center point of the outer surface of C2-4. This image reveals the differences in the damage effects caused by shock wave diffraction under different working conditions. The shock waves generated by the simultaneous explosion of multiple explosives cause the diffracted waves to act earlier on the side walls of the MCS. This is because during the propagation of underwater explosion shock waves, a larger wavefront pressure results in a faster shock wave velocity. Moreover, the pressure of the superimposed shock wave fronts is significantly greater than that of a single shock wave. Comparing working conditions 1 and 2, it can be concluded that an increase in explosive charge can significantly enhance the damage caused by the diffracted shock wave. Comparing working conditions-1 and -3 to -6, it can be seen that the diffraction of explosion shock waves generated by the simultaneous explosion of multiple explosives causes more severe damage to the MCS.

4.4.3 Damage effects of two-point explosions at different locations on MCS

To conduct an in-depth study on the damage effects of two-point explosions at different locations on MCS, the central deck surface of MCS was meticulously divided

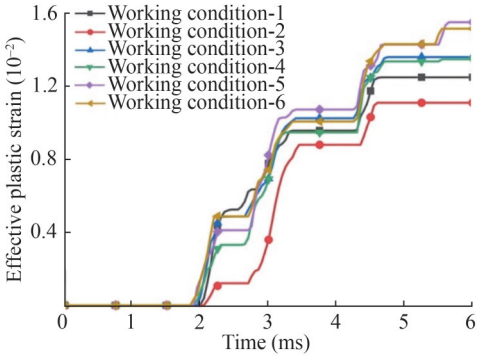


Figure 21 Equivalent plastic strain under different working conditions

into a 5 × 5 grid, totaling 25 points. The direct distance between two adjacent points in both the lateral and longitudinal directions is 10 cm. Figure 22 visually displays the number and specific location of each point. Based on this, to further reveal the damage effects resulting from explosions at different point combinations, a systematic numerical simulation analysis method was employed. Numerical simulation has been conducted for typical scenarios involving varying explosive charges, different explosion distances, and various explosive positions. The results are presented in Table 7.

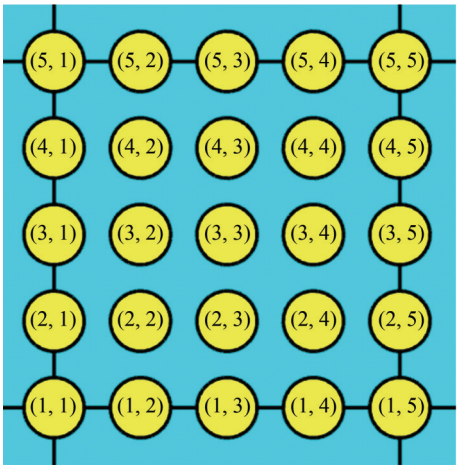


Figure 22 Explosive numbering for two-point explosion

Table 7 Damage results of two-point explosions at different locations

Explosive charge (g)	Explosion distance (cm)	Explosion 1	Explosion 2	Damage mode	Explosive charge (g)	Explosion distance (cm)	Explosion 1	Explosion 2	Damage mode
540	24	(1, 1)	(1, 2)	II	540	24	(1, 1)	(1, 3)	II
540	24	(1, 1)	(1, 4)	II	540	24	(1, 1)	(1, 5)	I
540	24	(1, 2)	(1, 3)	II	540	24	(1, 2)	(1, 4)	II
540	24	(2, 1)	(2, 2)	II	540	24	(2, 1)	(2, 3)	II
540	24	(2, 1)	(2, 4)	II	540	24	(2, 1)	(2, 5)	I
540	24	(2, 2)	(2, 3)	I	540	24	(2, 2)	(2, 4)	II
540	24	(3, 1)	(3, 2)	II	540	24	(3, 1)	(3, 3)	II

Table 7 Damage results of two-point explosions at different locations (continued)

Explosive charge (g)	Explosion distance (cm)	Explosion 1	Explosion 2	Damage mode	Explosive charge (g)	Explosion distance (cm)	Explosion 1	Explosion 2	Damage mode
540	24	(3, 1)	(3, 4)	II	540	24	(3, 1)	(3, 5)	I
540	24	(3, 2)	(3, 3)	I	540	24	(3, 2)	(3, 4)	II
540	24	(1, 1)	(2, 2)	II	540	24	(1, 1)	(3, 3)	II
540	24	(1, 1)	(4, 4)	II	540	24	(1, 1)	(5, 5)	I
540	24	(2, 2)	(3, 3)	I	540	24	(2, 2)	(4, 4)	II
540	24	(1, 2)	(2, 3)	II	540	24	(1, 2)	(3, 4)	II
540	24	(1, 2)	(4, 5)	II	540	24	(2, 3)	(3, 4)	I
540	24	(1, 3)	(2, 4)	II	540	24	(1, 3)	(3, 5)	II
540	24	(1, 4)	(2, 5)	II	540	24	(1, 1)	(2, 3)	II
540	24	(1, 1)	(2, 4)	II	540	24	(1, 1)	(2, 5)	I
540	24	(1, 1)	(3, 4)	II	540	24	(1, 1)	(3, 5)	I
540	24	(1, 1)	(4, 5)	I	540	24	(1, 2)	(2, 4)	II
540	24	(1, 2)	(2, 5)	II	540	24	(1, 2)	(3, 3)	II
540	24	(1, 2)	(3, 5)	II	540	24	(1, 2)	(4, 3)	II
540	24	(1, 2)	(4, 4)	II	540	24	(1, 2)	(5, 3)	I
540	24	(1, 2)	(5, 4)	I	540	24	(1, 3)	(2, 5)	II
540	24	(1, 3)	(3, 4)	II	540	24	(1, 3)	(4, 4)	II
540	24	(2, 2)	(3, 4)	II	540	28	(1, 1)	(1, 2)	I
540	28	(1, 1)	(1, 3)	I	540	28	(1, 1)	(1, 4)	I
540	28	(3, 1)	(3, 2)	II	540	28	(1, 1)	(3, 3)	I
540	28	(2, 2)	(4, 4)	II	540	32	(1, 1)	(1, 2)	I
540	32	(1, 1)	(1, 3)	I	540	32	(1, 1)	(1, 4)	I
540	32	(3, 1)	(3, 2)	I	540	32	(1, 1)	(3, 3)	I
540	32	(2, 2)	(4, 4)	I	540	20	(1, 1)	(1, 5)	II
540	20	(1, 1)	(2, 5)	II	540	20	(1, 1)	(3, 5)	II
540	20	(1, 1)	(4, 5)	I	540	20	(1, 1)	(5, 5)	I
270	14	(1, 1)	(1, 2)	II	270	14	(1, 1)	(1, 3)	II
270	14	(1, 1)	(1, 4)	II	270	14	(1, 1)	(1, 5)	I
270	14	(1, 1)	(3, 3)	II	270	14	(2, 2)	(4, 4)	I
270	14	(3, 1)	(3, 2)	II	270	16	(1, 1)	(1, 2)	I
270	16	(1, 1)	(1, 3)	I	270	16	(1, 1)	(1, 4)	I
270	16	(1, 1)	(1, 5)	I	270	16	(1, 1)	(3, 3)	II
270	16	(2, 2)	(4, 4)	I	270	16	(3, 1)	(3, 2)	II
270	18	(1, 1)	(1, 2)	I	270	18	(1, 1)	(1, 3)	I
270	18	(1, 1)	(1, 4)	I	270	18	(1, 1)	(1, 5)	I
270	18	(1, 1)	(3, 3)	I	270	18	(2, 2)	(4, 4)	I
270	18	(3, 1)	(3, 2)	I	1 080	32	(1, 1)	(1, 2)	II
1 080	32	(1, 1)	(1, 3)	II	1 080	32	(1, 1)	(1, 4)	II
1 080	32	(1, 1)	(1, 5)	II	1 080	32	(3, 1)	(3, 2)	II
1 080	32	(1, 1)	(3, 3)	II	1 080	32	(2, 2)	(4, 4)	II
1 080	36	(1, 1)	(1, 5)	II	1 080	36	(1, 1)	(5, 5)	I
1 080	36	(1, 1)	(2, 5)	II	1 080	36	(2, 2)	(4, 4)	II
1 080	36	(1, 1)	(3, 3)	II	1 080	36	(3, 1)	(3, 2)	II
1 080	36	(1, 1)	(3, 5)	II	1 080	40	(1, 1)	(1, 5)	II

Table 7 Damage results of two-point explosions at different locations (continued)

Explosive charge (g)	Explosion distance (cm)	Explosion 1	Explosion 2	Damage mode	Explosive charge (g)	Explosion distance (cm)	Explosion 1	Explosion 2	Damage mode
1080	40	(1, 1)	(1, 5)	II	1080	40	(1, 1)	(2, 5)	II
1080	40	(1, 1)	(2, 5)	II	1080	40	(1, 1)	(3, 3)	I
1080	40	(1, 1)	(3, 3)	I	1080	40	(1, 1)	(3, 5)	II
1080	40	(1, 1)	(3, 5)	II					

To thoroughly investigate the patterns of damage effects on MCS caused by different locations of explosives, a comprehensive analysis was conducted on the detailed damage results recorded in Table 7. The following inferences can be drawn: 1) The most significant factors influencing the shock wave pressure of explosives are the mass of the explosive and the distance of propagation. When the mass of the explosive is larger and the distance of action is closer, the damage effect is better. 2) Based on previous research, when the distance between two explosives is too close, the peak pressure of the resulting superimposed shock wave is relatively small. On the other hand, if the distance between the two explosives is too far, the shock wave pressure generated by each of them will significantly decrease, subsequently reducing the peak pressure of the superimposed shock wave. Therefore, there exists an optimal explosive spacing that maximizes the damage effect. 3) Further analysis of the damage results in Table 7 reveals that the locations of the explosives can be mainly classified into two categories: one is inside the cabin surface, and the other is at the edge of the cabin surface. Observing the damage process of MCS under the Mode II damage caused by the simultaneous explosion of two explosives, it was found that failure always first occurs in the middle part of the edge of the cabin surface. Subsequently, this initial breach gradually enlarges and connects at the corners of both edges of the cabin surface, forming a larger continuous breach, as shown in Figure 23. The different locations of the explosives mainly affect the position where the superimposed shock wave acts, thereby producing different damage effects on the structure.

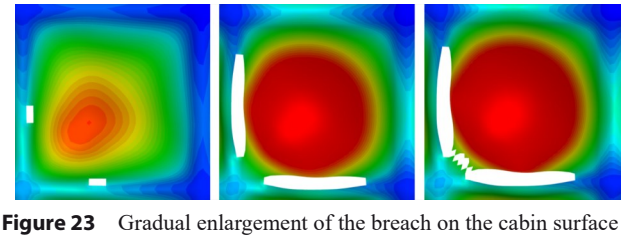


Figure 23 Gradual enlargement of the breach on the cabin surface

Based on the above inferences, an empirical equation is established to describe the damage effect of simultaneous explosions of two explosives on MCS, using F^* as the damage factor to differentiate damage modes. From inference 1), it can be concluded that F^* is related to the amount of explosive and the distance of the explosion. From inference 2), it can be concluded that F^* is related to the combined angle of the shock waves and the combined distance of the shock waves. From inference 3), it can be concluded that F^* is related to the positions of two explosives projected onto the MCS. The positions of the two explosives can be unified into three cases: L_I, where both explosives are on the edge of the surface; L_{II}, where one is on the edge and the other is inside; and L_{III}, where both are inside. Thus, the expression for F^* can be obtained as

$$R_S = \sqrt{R_E^2 + R_D^2} \tag{19}$$

$$\theta_S = \tan^{-1}\frac{2R_E}{R_D} \tag{20}$$

$$D^* = k \cdot W^{\alpha} \cdot R_E^{\beta} \cdot R_s^{\gamma} \cdot \cos^{\tau}\left(\left|\theta_S - \theta_0\right|\right) \tag{21}$$

In the equations, k is a constant coefficient; $\alpha, \beta, \gamma, \tau$ are exponential coefficients; W is the explosive mass, kg; R_E is the distance between the explosive and the MCS, m; R_D is the distance between the two explosives; R_s is the combined distance of the shock waves, m; θ_S is the combined angle of the shock waves; θ_0 is the optimal combined angle.

By fitting the results of all the conditions in Table 7, the parameters of F^* for three different positions are obtained, as shown in Table 8.

Table 8 The parameters for three different explosion locations in Equation (20)

	k	α	β	γ	τ	θ_0
L_I	7.435	1.452	−1.21	−0.820	1.89	1.152
L_{II}	4.640	1.742	−2.15	−1.030	1.05	1.117
L_{III}	1.550	2.162	−2.15	−0.653	2.20	1.012

When utilizing the parameters from Table 8, one simply needs to substitute the explosive charge weight, the distance of the explosion, and the position of the explosive into Equation (20) to obtain the damage factor F^*. If $F^* \geqslant 1$, the explosive will cause Mode II damage to the MCS; if $F^* < 1$, the explosive will cause Mode I damage to the MCS. The damage factor F^* was employed to predict the numeri-

cal simulation scenarios outlined in Table 7, yielding an impressive prediction accuracy of 96.5%.

5 Conclusion

Through experimental research, this paper comprehensively analyzes the damage characteristics of different decks of multi-cabin structure (MCS) under near-field underwater explosion. Based on the validation of the effectiveness of numerical simulation, the dynamic damage process of the MCS is analyzed, and the responses of the MCS under different explosion conditions are compared. The specific conclusions of this study are as follows:

1) Under the action of near-field underwater explosion, the different cabins of the MCS exhibited differentiated damage situations. The four cabins closest to the explosion source suffered the most severe damage, resulting in large breach damage effects. The remaining five cabins all experienced significant plastic deformation. The deformation of each cabin was not entirely the same, which was related to the relative position between the cabin and the explosive, as well as the position of the cabin in the MCS.

2) When the shock wave reaches the first layer cabin surface, transmission occurs. The transmitted shock wave will cause damage to the second layer cabin surface. After the first layer cabin surface is breached by the shock wave, water will enter the cabin and generate a jet, which will act on the second layer cabin surface and cause it to undergo more severe plastic deformation.

3) There are three main damage modes for the MCS: I) Plastic deformation of the first layer; II) Tearing failure of the first layer with large deformation of the second layer; III) Tearing failure of both the first and second layers. Different explosive positions and shock wave impact locations can result in different damage modes. When the shock wave acts on the corner, Mode II is more prone to occur, whereas when the shock wave acts on the center, Mode III tends to emerge.

4) At the same explosion distance, compared to a single 1 080 g TNT explosive, the shock wave resulting from the simultaneous detonation of two 540 g TNT explosives causes greater damage to the area situated between the explosives in the MCS, whereas the damage to the areas on the outer sides of the explosives is comparatively less significant.

5) A damage factor F^* is introduced to determine the damage mode of MCS under the simultaneous explosion of two explosives. F^* is related to the amount of explosive, the distance from the explosion, the spacing between explosives, and the projection position of the explosives on the MCS. When $F^* \geqslant 1$, MCS experiences damage in Mode II; whereas when $F^* < 1$, MCS undergoes damage in Mode I. F^* achieves 96.5% accuracy in damage mode prediction for MCS under 250 g–1 080 g TNT charges.

Funding The National Natural Science Foundation of China (Grant No. 12372361).

Competing interest The authors have no competing interests to declare that are relevant to the content of this article.

References

Achor CH, Kwon YW, Didoszak JM, Crow NE, Hardman DJ (2022) Study of air-backed and water-backed carbon fiber composite plates subjected to underwater shock loading. Composite Structures, 300: 116147. https://doi.org/10.1016/j.compstruct.2022.116147

Bonorchis D, Nurick GN (2010) The analysis and simulation of welded stiffener plates subjected to localised blast loading. International Journal of Impact Engineering, 37(3): 260-273. https://doi.org/10.1016/j.ijimpeng.2009.08.004

Chen Z, Zong Z, Gan L, Li M, Liu L, Qian H (2023) Numerical investigation on dynamic response of air-backed RC slabs subjected to close-in underwater explosion. Ocean Engineering, 273: 113962. https://doi.org/10.1016/j.oceaneng.2023.113962

Chung KYS, Nurick GN (2005) Experimental and numerical studies on the response of quadrangular stiffened plates. Part I: subjected to uniform blast load. International Journal of Impact Engineering, 31(1): 55-83. https://doi.org/10.1016/j.ijimpeng.2003.09.048

Cole RH (1948) Underwater explosions. Princeton: Princeton Univ. Press

Costanzo FA (2012) A closed form solution to the early-time underwater explosion (UNDEX) response of a rectangular air-backed ship hull panel. Paper presented at the Topics in Modal Analysis II, Volume 6, New York

Gao H, Tian H, Gao X (2023) Damage characteristics of cabin in navigational state subjected to near-field underwater explosion. Ocean Engineering, 277: 114256. https://doi.org/10.1016/j.oceaneng.2023.114256

He Z, Chen Z, Jiang Y, Cao X, Zhao T, Li Y (2020) Effects of the standoff distance on hull structure damage subjected to near-field underwater explosion. Marine Structures, 74: 102839. https://doi.org/10.1016/j.marstruc.2020.102839

He Z, Du Z, Zhang L, Li Y (2023) Damage mechanisms of full-scale ship under near-field underwater explosion. Thin-Walled Structures, 189: 110872. https://doi.org/10.1016/j.tws.2023.110872

Henchie TF, Chung KYS, Nurick GN, Ranwaha N, Balden VH (2014) The response of circular plates to repeated uniform blast loads: An experimental and numerical study. International Journal of Impact Engineering, 74: 36-45. https://doi.org/10.1016/j.ijimpeng.2014.02.021

Jen C, Tai YS (2010) Deformation behavior of a stiffened panel subjected to underwater shock loading using the non-linear finite element method. Materials & Design, 31(1): 325-335. https://doi.org/10.1016/j.matdes.2009.06.011

Jin J, Hou H, Chen P, Zhu X, Li D (2019) Experimental study on the combined damage of liquid cabin structure subjected to charge explosion with preset fragments. International Journal of Impact Engineering, 130: 19-26. https://doi.org/10.1016/j. ijimpeng.2019.04.001

Jones N (2011) Structural Impact(M). Cambridge: Cambridge University Press

Li H, Zhang C, Zheng X, Mei Z, Bai X (2021a) A simplified theoretical model of the whipping response of a hull girder subjected to underwater explosion considering the damping

effect. Ocean Engineering, 239: 109831. https://doi.org/10.1016/j.oceaneng.2021.109831

Li Y, Ren X, Zhao T, Xiao D, Liu K, Fang D (2021b) Dynamic response of stiffened plate under internal blast: Experimental and numerical investigation. Marine Structures, 77: 102957. https://doi.org/10.1016/j.marstruc.2021.102957

Lin S, Wang J, Liu L, Li H, Ma T, Tang K (2021) Research on damage effect of underwater multipoint synchronous explosion shock waves on air-backed clamped circular plate. Ocean Engineering, 240: 109985. https://doi.org/10.1016/j.oceaneng.2021.109985

Qin Y, Yao X, Wang Z, Wang Y (2022) Experimental investigation on damage features of stiffened cabin structures subjected to internal blast loading. Ocean Engineering, 265: 112639. https://doi.org/10.1016/j.oceaneng.2022.112639

Rajendran R, Lee JM (2008) A comparative study of air- and water-backed plated subjected to non-contact underwater explosion International Journal of Modern Physics B, 22(09n11): 1311-1318. https://doi.org/10.1142/S0217979208046700

Tian S, Du X, Yan Q, Wu J, Zhuang T (2023) Damage effect of pile wharf under underwater explosion load. Mechanics of Advanced Materials and Structures, 30(1): 29-47. https://doi. org/10.1 080/15376494.2021.2006840

Truong DD, Jang BS, Ju HB (2021) Development of simplified method for prediction of structural response of stiffened plates under explosion loads. Marine Structures, 79: 103039. https://doi.org/10.1016/j.marstruc.2021.103039

Wu W, Liu M, Zhang A, Liu, Y (2021) Fully coupled model for simulating highly nonlinear dynamic behaviors of a bubble near an elastic-plastic thin-walled plate. Physical Review Fluids, 6(1): 013605. https://doi.org/10.1103/PhysRevFluids.6.013605

Wu W, Liu Y, Zhang A, Liu M (2022) An h-adaptive local discontinuous Galerkin method for second order wave equation: Applications for the underwater explosion shock hydrodynamics. Ocean Engineering, 264: 112526. https://doi.org/10.1016/j.oceaneng.2022.112526

Wu W, Liu Y, Zhang A, Liu N, Liu L (2020) Numerical investigation on underwater explosion cavitation characteristics near water wave. Ocean Engineering, 205: 107321. https://doi.org/10.1016/j.oceaneng.2020.107321

Zhang A, Li S, Cui P, Li S, Liu YL (2023) A unified theory for bubble dynamics. Physics of Fluids, 35(3): 033323. https://doi.org/10.1063/5.0145415

Zhang A, Yang W, Yao X (2012) Numerical simulation of underwater contact explosion. Applied Ocean Research, 34: 10-20. https://doi.org/10.1016/j.apor.2011.07.009

Zhang Y, Guo J, Hao N, Yang J, Li S (2020) Damage detection on hull girder of ship subjected to explosion loading. Ocean Engineering, 198: 107006. https://doi. org/10.1016/j. oceaneng. 2020. 107006

Zhao N, Yao S, Zhang D, Lu F, Sun C (2020) Experimental and numerical studies on the dynamic response of stiffened plates under confined blast loads. Thin-Walled Structures, 154: 106839. https://doi.org/10.1016/j.tws.2020.106839

Zhou H, Kong X, Wang Y, Zheng C, Pei Z, Wu W (2021) Dynamic response of hull girder subjected to combined underwater explosion and wave induced load. Ocean Engineering, 235: 109436. https://doi.org/10.1016/j.oceaneng.2021.109436

Zhou J, Zhi X, Xu J, Yue Z (2019) Research on penetration of small size fragment to single soldier protection equipment. Explosion and Shock Waves, 39(2): 023304 (in Chinese). https://doi.org/10.11883/bzycj-2018-0023

Zhou L Li X, Yan Q (2024) Dynamic response and vulnerability analysis of pier under near-field underwater explosion. Engineering Failure Analysis, 155, 107749. https://doi.org/10.1016/j.engfailanal.2023.107749